

# Helium implantation in Si (100): Swelling, microstructure, and mechanical property changes

Cite as: J. Appl. Phys. 132, 025106 (2022); doi: 10.1063/5.0096802

Submitted: 21 April 2022 · Accepted: 7 June 2022 ·

Published Online: 13 July 2022



View Online



Export Citation



CrossMark

Xi Huang,<sup>1</sup> Yujun Xie,<sup>1,2,a)</sup> Mehdi Balooch,<sup>1</sup> Sean Lubner,<sup>3,4</sup> and Peter Hosemann<sup>1,5,a)</sup>

## AFFILIATIONS

<sup>1</sup>Department of Nuclear Engineering, University of California Berkeley, Berkeley California 94704, USA

<sup>2</sup>National Center for Electron Microscopy, Molecular Foundry, Lawrence Berkeley National Laboratory, Berkeley, California 94720, USA

<sup>3</sup>Energy Storage and Distributed Resources Division, Lawrence Berkeley National Laboratory, Berkeley, California 94720, USA

<sup>4</sup>Research Laboratory of Electronics, Massachusetts Institute of Technology, Cambridge, Massachusetts 02139, USA

<sup>5</sup>Materials Sciences Division, Lawrence Berkeley National Laboratory, Berkeley, California 94720, USA

**Note:** This paper is part of the Special Topic on Radiation Effects in Materials.

**a) Authors to whom correspondence should be addressed:** terryxie007@lbl.gov and peterh@berkeley.edu

## ABSTRACT

Microstructural changes induced by helium implantation in materials lead to volumetric swelling and mechanical property changes. How these properties are linked and establishing direct relationships can be difficult due to the underlying material's microstructure evolution. Some materials also experience a phase change due to irradiation damage making them even more complex to analyze. Here, single crystalline Si (100) was used to establish a relationship among these parameters. The swelling height as a function of implantation fluence can equally fit a linear relationship. Solely irradiation induced defects are observed at low fluence below  $5.0 \times 10^{16}$  ions/cm<sup>2</sup>. An abrupt amorphous and crystalline mixed layer of ~200 nm thick within a highly damaged polycrystalline matrix is observed when implantation fluence exceeds  $5.0 \times 10^{16}$  ions/cm<sup>2</sup>, leading to the appearance of irradiation induced swelling and hardening behavior. As the fluence increases beyond  $1.0 \times 10^{17}$  ions/cm<sup>2</sup>, the amorphous layer expands in size and the bubble size distribution takes the form of a Gaussian distribution with a maximum size of up to 6.4 nm, which causes a further increase in the height of swelling. Furthermore, irradiation induced softening appeared due to the enlarged bubble size and amorphization.

Published under an exclusive license by AIP Publishing. <https://doi.org/10.1063/5.0096802>

24 August 2023 06:54:15

## I. INTRODUCTION

Ion irradiation techniques are widely employed to evaluate the irradiation damage and swelling behavior of materials in nuclear applications because they can generate high damage rates without significant residual radioactivity and at a lower cost compared to neutron irradiation.<sup>1,2</sup> The technique has also been adopted as a tool to introduce controllable concentrations of defects at precise depths in the semiconductors field.<sup>3</sup> The introduction of defects will lead to changes in the microstructure of semiconductor and insulator materials, resulting in a wide variation in physical behaviors, including electrical and optical properties.<sup>4</sup> Small irradiating beam spot sizes also allow heterogeneous alterations of mechanical properties with <10 nm resolution. This could enable new approaches to creating cryogenic phononic metamaterials by

patterning sub-wavelength features,<sup>5–7</sup> such as to shield qubits from deleterious phonons in quantum computers or increase the detection efficiency of dark matter detectors by better guiding collision-generated phonons to detectors. Therefore, major efforts have been made to understand the effect of ion irradiation in the semiconductor materials field in the past few decades, especially on Si, the most important material in the semiconductor industry today.<sup>3,8,9</sup>

The formation of helium bubbles in Si due to ion beam implantation was first reported by Griffioen *et al.*<sup>10</sup> Since then, the underlying mechanisms and their possible applications in the semiconductor industry have extensively been investigated.<sup>11</sup> Summarizing the previous research results, it is found that the formation of He bubbles in Si is affected by multiple factors: implantation dose, dose rate, energy,<sup>12,13</sup> temperature,<sup>14,15</sup> and post-implantation thermal treatments<sup>16,17</sup> among

others. The formation of bubbles is accompanied by the change of the density of Si, which will result in swelling.<sup>18–21</sup> Momota *et al.* investigated the swelling behavior of Si under Ar<sup>+</sup> implantation and concluded that swelling height increases with the increasing of implantation fluence and energy.<sup>20</sup> Zhang *et al.* studied the annealing temperature on the swelling behavior of Ar<sup>+</sup> implanted Si and reported that swelling height varies with annealing temperature.<sup>21</sup> Ikeyama *et al.* found that He implantation induced swelling becomes saturated over  $1.0 \times 10^{15}$  ions/cm<sup>2</sup> regardless of implantation energy, and the maximum swelling height is almost proportional to implantation fluence.<sup>18</sup> So far, the swelling behavior of Si under He implantation has been, however, examined at the lower limits of implantation fluences: such as  $8.0 \times 10^{16}$ ,<sup>21</sup>  $8.0 \times 10^{16}$ ,<sup>20</sup>  $6.0 \times 10^{16}$ ,<sup>19</sup> and  $1\text{--}2.0 \times 10^{17}$  ions/cm<sup>2</sup>.<sup>18</sup> The swelling behavior of Si is still unknown when implantation fluence reaches a higher level of about  $1.0 \times 10^{18}$  ions/cm<sup>2</sup> or beyond. Of particular interest is finding a correlation between volumetric swelling and changes in micromechanical and thermal properties of single-crystal Si under He implantation. Conducting the study on a single crystal allows studying the effects without the influence of underlying microstructure such as grain boundaries that further complicates the studies.

The current work presents a relationship among the swelling height, microstructure, and corresponding micromechanical properties of a single-crystal Si under He implantation beyond the range of fluences reported before. The Si (100) was implanted by 25 keV He with the fluences of  $5.0 \times 10^{16}$ ,  $1.0 \times 10^{17}$ ,  $2.0 \times 10^{17}$ ,  $5.0 \times 10^{17}$ ,  $7.5 \times 10^{17}$ , and  $1.0 \times 10^{18}$  ions/cm<sup>2</sup>. Following implants, the swelling behavior, microstructure, and micromechanical properties of implanted Si were evaluated by advanced techniques of AFM, SEM, and TEM.

## II. EXPERIMENTAL PROCEDURES

A high-purity (>99.99%) undoped single-crystal Si (100) sample was used as the target in this investigation. The helium implantation experiments were conducted at room temperature (RT) using the focused helium ion beam of a Zeiss ORION NanoFab HIM operated at 25 keV. The ion beam had a few nanometers that scanned over the sample with a diameter incident perpendicular to the surface. The sputtering yield of a 25 keV beam on Si was less than  $5 \times 10^{-2}$ .<sup>22</sup> The implants were performed at different fluences covering order of magnitude, each covering  $10 \times 10 \mu\text{m}^2$  areas on the same sample. The beam current was maintained at  $\sim 100$  pA during implants while reduced to  $\sim 1$  pA for imaging to avoid significant additional implants. The profile of displacement damage in units of displacement per atom (dpa) and ions distribution was calculated using the Stopping and Range of Ions in Matter (SRIM-2013) code based on the full damage cascades (F-C) model.<sup>23</sup> The threshold displacement energy, lattice binding energy, and surface binding energy used in this investigation were 40, 3.25, and 4.7 eV, respectively.<sup>24</sup> The SRIM use in the present studies, however, does not account for porosity, crystal orientation, or structure. The displacement damage profile and ion distribution in Si (100) implanted with a total fluence of  $1.0 \times 10^{17}$  and  $1.0 \times 10^{18}$  ions/cm<sup>2</sup> are shown in Fig. 1. The peak values of He concentration are  $1.1 \times 10^5$  and  $1.1 \times 10^6$  atomic parts per million

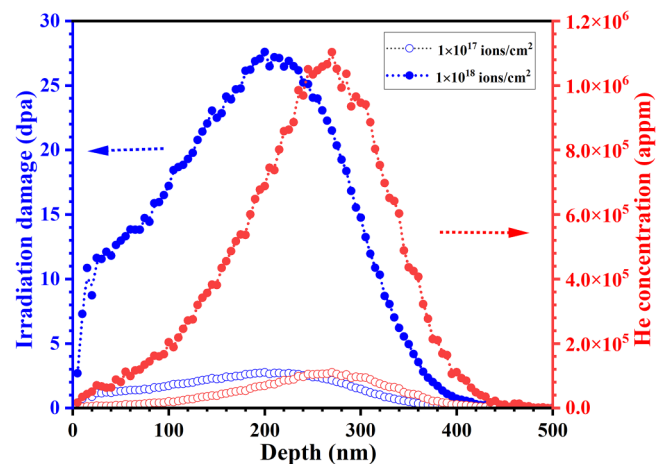


FIG. 1. The displacement damage profile and ions distribution in Si (001) subjected to He ion implantation at 25 keV with different fluences.

(appm) at a depth of  $\sim 275$  nm for doses of approximately 2.8 and 27.6, respectively.

Atomic force microscopy (AFM), Nanoscope III made by Digital Instruments Inc., was used to analyze the changes in surface topography, roughness, and swelling. Following the AFM imaging, the irradiated sample was attached firmly to an iron puck using a crystal bond and subsequently mounted on the magnetic stage of TI950. The mechanical properties of the samples within and off implanted areas were tested using a Hysitron TI 950 TriboIndenter using a diamond Berkovich indenter tip with a nominal radius of curvature of 50 nm that was calibrated in advance against fused silica. The continuous stiffness measurement (CSM) mode was employed to test the hardness and elastic modulus of implanted samples at different depths. The maximum penetration depth is controlled between 200 and 250 nm in the present investigation. For each area, nine indentations were taken to obtain the average hardness and elastic modulus and their standard deviations.

Thin-foil samples for transmission electron microscope (TEM) were prepared using a Helios NanoLab 600i dual-beam focused ion beam (DB-FIB) with a Ga ion sputtering after a protective Pt layer was deposited on the implanted area. Microstructure and selected area electron diffraction (SAED) analysis were conducted on 300 kV JEOL 3010 at the national center for electron microscopy of Lawrence Berkeley National Laboratory.

## III. RESULTS AND DISCUSSIONS

Figure 2 shows the AFM surface topographic images and corresponding swelling height of implanted areas with different fluences ranging from  $1.0 \times 10^{17}$  to  $1.0 \times 10^{18}$  ions/cm<sup>2</sup>. The swelling height of samples implanted with  $5.0 \times 10^{16}$  ions/cm<sup>2</sup> is not illustrated in Fig. 2 because the swelling height was below the uncertainty level of AFM measurements in our laboratory. The outline of the implanted area gradually becomes clear with the increase of fluences, indicating that swelling height gradually increases with the

24 August 2023 06:54:15

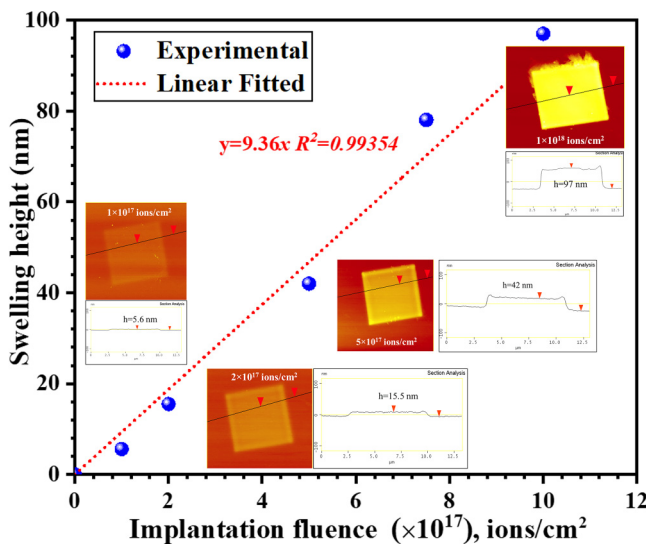


**FIG. 2.** AFM surface topographic images and corresponding swelling height of implanted areas with different fluences ranging from  $1.0 \times 10^{17}$  to  $1.0 \times 10^{18}$  ions/cm $^2$ .

rise of implantation fluences. The swelling height of the edge region measures higher than that of the middle region: for example, the former is 47 nm for  $5.0 \times 10^{17}$  ions/cm $^2$  and the latter is 42 nm. Furthermore, the difference between these two regions gradually increases with increasing fluences, except for  $1.0 \times 10^{18}$  ions/cm $^2$  where no measurable differences are observed. Because He bubbles are not formed at low implantation fluences, the phenomenon may be due to the stress concentration caused by volume change during the amorphization process. Amorphous transformation leads to severe distortion of the lattice,<sup>25</sup> resulting in swelling. Swelling will bring a high stress concentration in the irradiated regions.<sup>26</sup> In order to relax the stress, the stress gradually concentrates at the edge region and then leads to a high swelling height. The sample implanted with high fluences results in the formation of high pressure bubbles that facilitates expansion in the direction normal to the surface more effectively.<sup>27</sup> Therefore, the excessive edge height effect diminishes.

Average values of 5.6, 15.5, 42.0, and 97.0 nm are evaluated for the fluences of  $1.0 \times 10^{17}$ ,  $2.0 \times 10^{17}$ ,  $5.0 \times 10^{17}$ , and  $1.0 \times 10^{18}$  ions/cm $^2$ , respectively. It appears that the swelling height as a function of fluence follows a linear relationship, as shown in Fig. 2. This result is different from that reported by Giri *et al.*, who investigated the swelling mechanism of Si under low energy self-ion irradiation (80 keV) and found that the swelling height follows a linear relationship with a cube root dependence on the fluences.<sup>19</sup> Eichler *et al.* investigated the defects in Si after B $^{+}$  implantation and reported that the defect concentration increases proportionally to the square root of the fluences.<sup>29</sup> What is more, Sealy *et al.* further confirmed this result by measuring the integrated strain of

Si by x-ray diffraction.<sup>30</sup> Besides, the results of Giri *et al.* revealed that the cube root relationship is caused by the effect of concentration of vacancy type defects in Si and found no irradiation induced amorphization and He bubbles formation in their studies.<sup>19</sup> However, the fluence of the self-ions there was rather low ( $6.0 \times 10^{16}$  ions/cm $^2$ ) and, therefore, only the generation of vacancies is considered. In the present work, we experience the effect of helium bubble formation, amorphization, and the generation of vacancies individually, depending on a range of ion fluence applied. Previous investigations have confirmed that the existence of helium bubbles and the amorphous layer will lead to the swelling of Si.<sup>31</sup> For example, Abrams *et al.* studied the helium irradiation effects in polycrystalline Si, and directly observed the increase in the width of the Si layer due to the microstructure change of He bubbles.<sup>31</sup> Meanwhile, the swelling behavior of SiC under helium implantation was studied by Leclerc *et al.*, and they reported that the contribution of amorphous to the swelling height is about 15% of the amorphous layer thickness.<sup>28</sup> It is known that the density of amorphous Si is 1.8% lower than that of crystalline Si,<sup>32</sup> which would lead to  $\sim 7$  nm height increase assuming the entire penetration depth amorphized. This seems to be close to the magnitude for  $1.0 \times 10^{17}$  ions/cm $^2$  implantation. It is worth mentioning in the present study that no blistering is observed even if the implantation fluence reaches  $1.0 \times 10^{18}$  ions/cm $^2$ . It may be possible that the threshold at which blistering occurs is beyond the maximum dose we used here, unlike metals such as W reported recently by Allen *et al.*, due to the limited ductility of the material.<sup>33</sup>

Figure 3 displays the cross-sectional TEM images and corresponding selected area electron diffraction (SAED) patterns of Si implanted with He ions to a fluence of  $5.0 \times 10^{16}$  ions/cm $^2$ . No detectable He bubbles are observed, while irradiation induced defects are visible in bright-field TEM, as shown in Fig. 3(a). The absence of helium bubbles indicates that irradiation induced bubbles in Si are in the stage of nucleation or perhaps incubation rather than growth. Besides, SAED patterns in the implanted area, as shown in Fig. 3(b), also reveal that no irradiation induced amorphization occurs as the irradiation fluence increases up to  $5.0 \times 10^{16}$  ions/cm $^2$ . Weak diffuse rings are observed on both implanted and unimplanted regions, as shown in Figs. 3(b) and 3(c). This may be the artificial feature caused by FIB preparation of the TEM slice rather than by ion irradiation. Previous investigations on the crystalline to amorphous transition in Si under He implantation also reported a similar result, though different experiments show slightly different threshold fluence to occur.<sup>34–36</sup> For instance, no irradiation induced amorphization was observed in Si implanted with He at energies between 20 and 300 keV with the fluence less than  $1.0 \times 10^{17}$  ions/cm $^2$ .<sup>34</sup> But, an amorphized layer was formed when a fluence of  $2.5 \times 10^{17}$  He atoms/cm $^2$  at 20 keV was implanted into Si at RT.<sup>35</sup> Summarizing the results of these experiments, it can be found that the amorphization of Si occurs for a fluence near  $1.0 \times 10^{17}$  cm $^{-2}$ . Besides, it should also be pointed out that most of the investigations on the amorphization of Si only state a fluence and rough numbers to quantify this behavior rather than dpa.<sup>34–36</sup> In current experiments, the maximum dpa at a fluence of  $5.0 \times 10^{16}$  ions/cm $^2$  is about 1.4 dpa, and, therefore, we can infer that the threshold of amorphization in Si should be larger than the above-mentioned value.

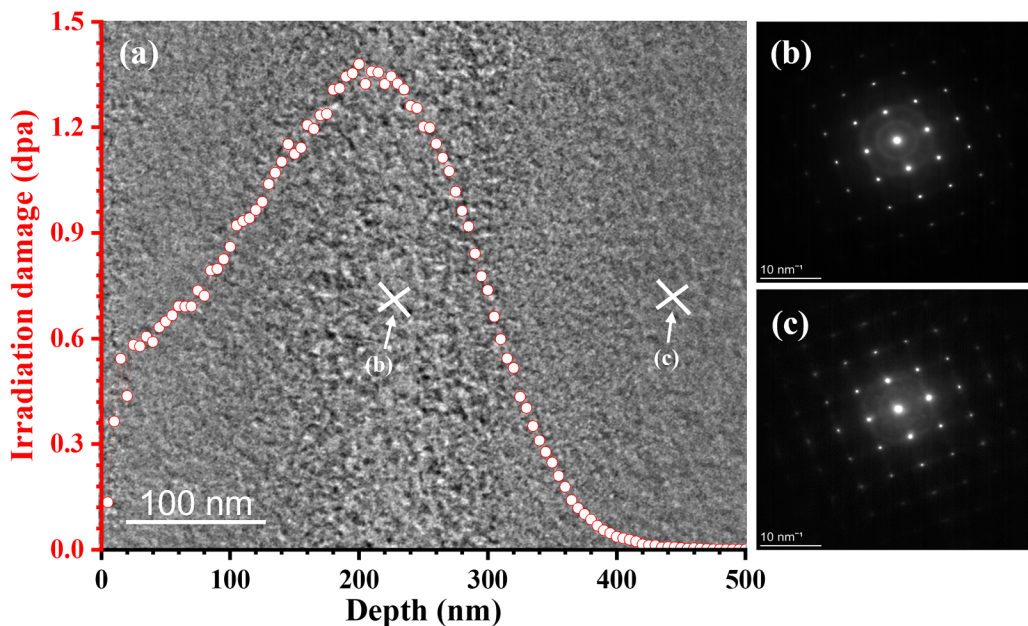


FIG. 3. The cross-sectional TEM image and corresponding SAED patterns of Si implanted with He to a fluence of  $5.0 \times 10^{16}$  ions/cm<sup>2</sup>: (a) the cross-sectional TEM image of implanted layer and (b) and (c) the SAED patterns at different positions marked in image (a).

24 August 2023 06:54:15

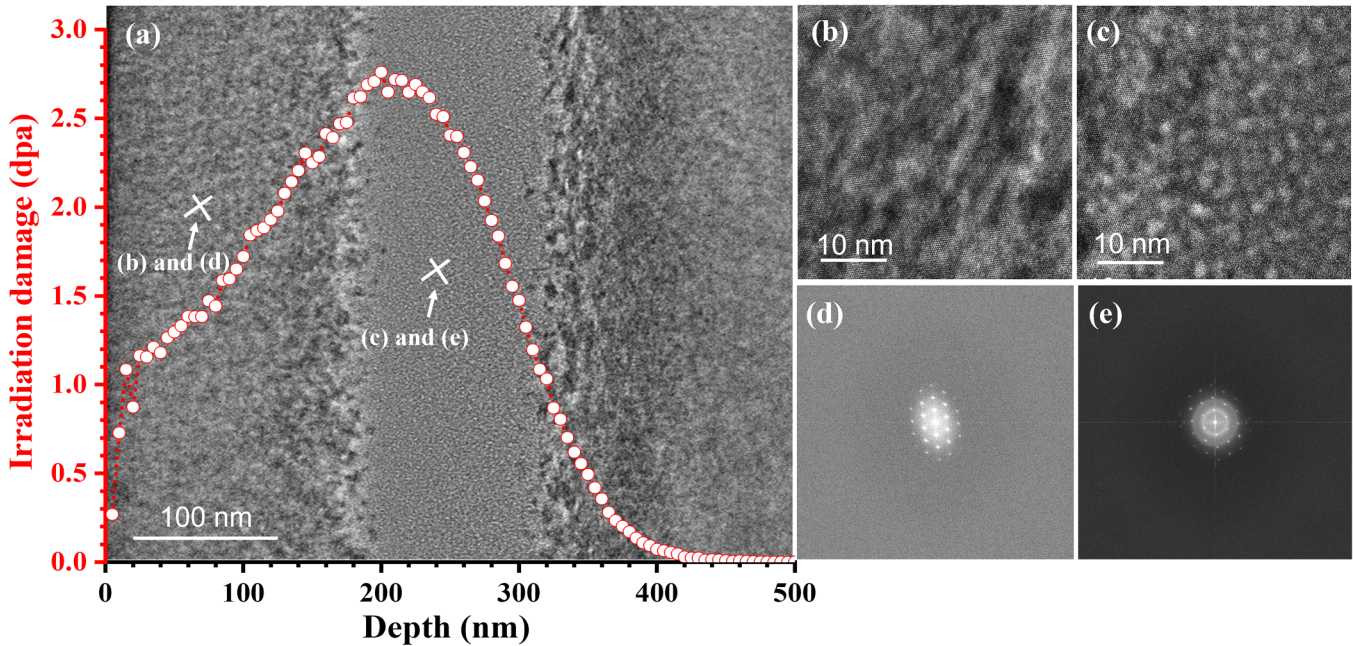
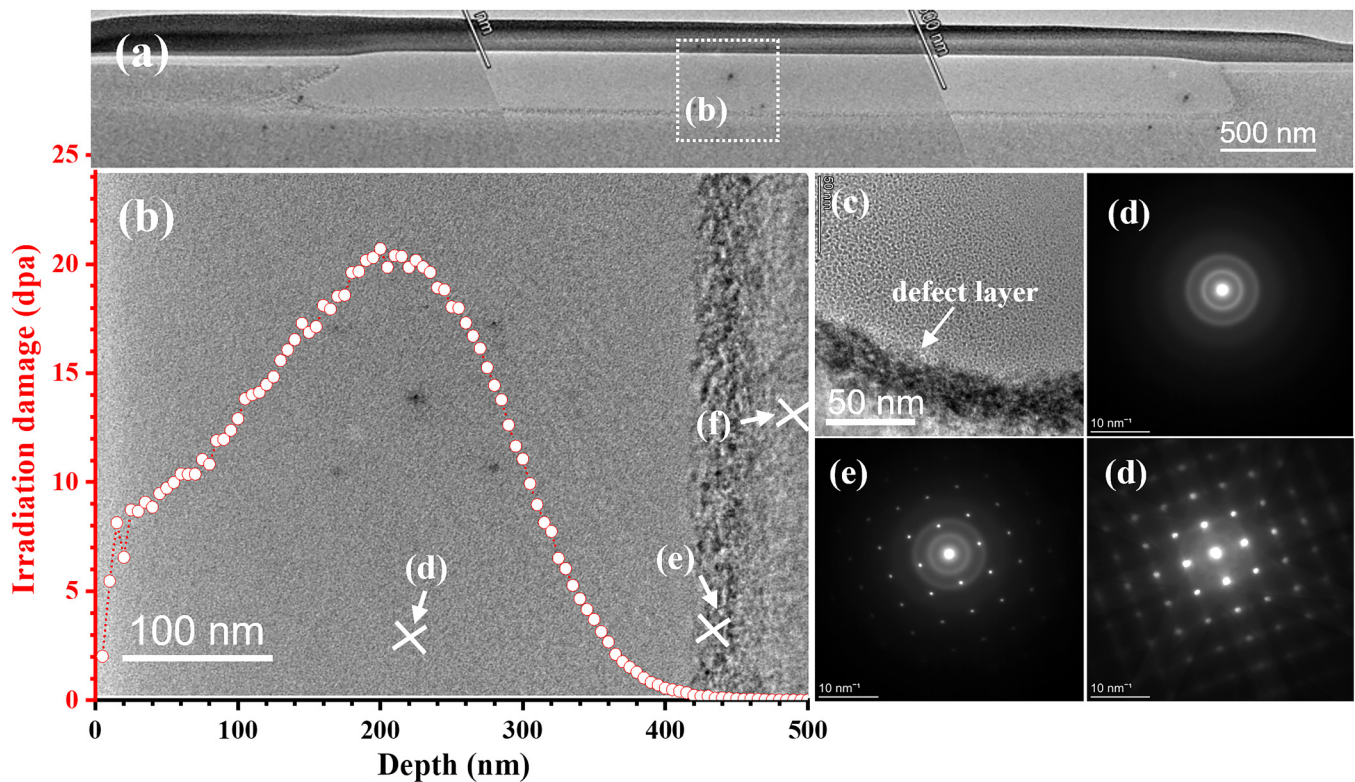


FIG. 4. The cross-sectional TEM images and corresponding FFT patterns of Si implanted with He ions to a fluence of  $1.0 \times 10^{17}$  ions/cm<sup>2</sup>: (a) the cross-sectional TEM images of implanted layer; (b) and (d) the enlarged image marked in image (a) and corresponding FFT pattern; and (c) and (e) the enlarged images marked in image (a) and corresponding FFT pattern.



**FIG. 5.** The cross-sectional TEM images and corresponding SAED patterns of Si implanted with He ions to a fluence of  $7.5 \times 10^{17}$  ions/cm<sup>2</sup>. (a) low magnification TEM image of the implanted area; (b) the enlarged image of position (b) marked in image (a); (c) the enlarged image at the end of the implantation range; and (d)–(f) the SAED patterns located at different positions marked in image (b).

24 August 2023 06:54:15

Figure 4 displays the cross-sectional TEM images and corresponding Fast Fourier Transform (FFT) patterns of Si implanted with He ions to a fluence of  $1.0 \times 10^{17}$  ions/cm<sup>2</sup>. An obvious band of about 200 nm appears at the peak of irradiation damage, as shown in Fig. 4(a). A larger number of bubbles are observed in this “band,” as shown in Figs. 4(a) and 4(c). The average size of the bubbles is around 1–2 nm when the TEM image is further enlarged, as shown in Fig. 4(c), and they are uniformly distributed within the “band.” The formation of a void layer free of any interstitial-type defects in Si was also reported by David *et al.*, who investigated the stability of defects created by high fluence helium implantation (50 keV,  $5.0 \times 10^{16}$  ions/cm<sup>2</sup>) from RT to 800 °C.<sup>37</sup> However, Haynes found the formation of a mixed layer of defects and helium bubbles in Si implanted with helium of fluence of  $4.0 \times 10^{16}$  ions/cm<sup>2</sup> at 0.5 keV and RT.<sup>38</sup> The difference may be attributed to the implantation energy and rate differences between their work and the present investigation. The higher the implantation energy and the rate, the larger the He bubble and lower density formation are expected.<sup>38</sup> An increase in the size of bubbles will absorb more vacancies and interstitial clusters, resulting in a low number of defects around He bubbles.

The “band” contains mixed amorphous and undisturbed matrix layers as evident from FFT analysis of high-resolution

electron microscopy, as shown in Fig. 4(e). This result suggests that the helium implantation partially induces the amorphization of single-crystal Si around a fluence of  $1.0 \times 10^{17}$  ions/cm<sup>2</sup>. This is in good agreement with the results of Reutov and Sokhatskii,<sup>36</sup> who also suggested a threshold of  $10^{17}$  ions/cm<sup>2</sup> at RT. In addition, Morehead and Crowder proposed that the critical temperature to occur the transition from crystalline to amorphous in Si by B<sup>+</sup> implantation is 33 °C.<sup>39</sup> Therefore, it can be inferred that the critical temperature for current experiments should be higher than B<sup>+</sup> implantation because He is lighter than B.<sup>35</sup> However, in the current work, amorphization takes place in Si implanted at RT, which is lower than expected. It has been established that the amorphous region is formed in the atomic collision cascades according to the principal accumulation of irradiation induced defects that will favor the amorphization of Si.<sup>36</sup> In current work, the low temperature of implantation ensures a low rate of the pair recombination of defects, leading to the formation of an amorphous layer. No obvious irradiation induced bubbles and amorphization is observed in the areas outside the end of the range for the ions areas, marking the dose level at which amorphization occurs between 1–3 dpa and 3 at. %He, as shown in Fig. 4.

The cross-sectional TEM micrographs and SAED patterns of the implanted sample with  $7.5 \times 10^{17}$  ions/cm<sup>2</sup> He ions are shown

in Fig. 5. Figure 5(a) shows a low magnification TEM image of the implantation region, in which an obviously amorphous layer is observed along perpendicular to the implantation direction. The swelling height of 78.0 nm is deduced from the cross section of the thin slice taken from the interface between the irradiated/unirradiated zone. According to the enlarged TEM images, Figs. 5(b) and 5(c), and SAED patterns, it can be found that three distinct zones are clear for this fluence: amorphous layer with a bubble size of 1–2 nm in diameters, defect layer, and matrix. It is well known that multiple aspects including irradiation induced phase transformation, generated defects, and implanted ions are contributed to the swelling of Si with He implantation.<sup>28</sup> The amorphous layer decreases the density of Si and, therefore, contributes to swelling.<sup>40,41</sup> Furthermore, the formation of bubbles also contributes to the swelling height of Si. The estimated swelling height

contribution from the amorphous phase transformation is estimated to be 7 nm based on the density change of amorphous Si.<sup>32</sup> Therefore, it can be inferred that the contribution of the swelling height from the bubbles should be 71 nm. To summarize the above statements, the current results show that the swelling is mainly attributed to the bubble formation.

The cross-sectional micrographs and corresponding SAED patterns of Si (001) implanted with the highest fluence ( $1.0 \times 10^{18}$  ions/cm<sup>2</sup>) are exhibited in Fig. 6. The TEM images display that He implantation induced the formation of bubbles, and the density and size of these bubbles vary with depth. The total damage layer in Si (100) is measured to be 447 nm from the TEM images, as shown in Fig. 6(a), while it is about 420 nm from the results of SRIM. The apparent discrepancy is attributed to the increment in the porosity of Si with the enhanced He

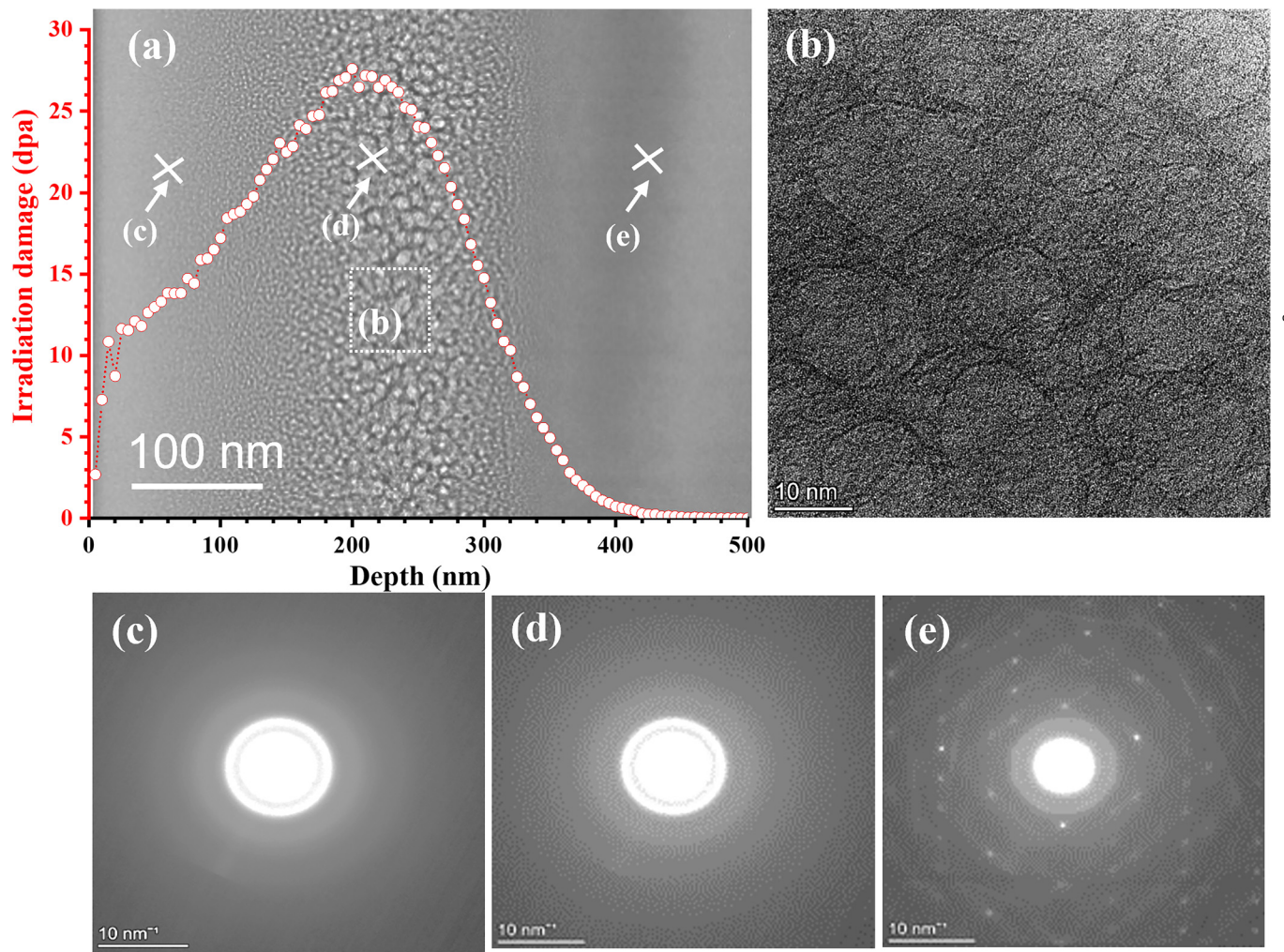
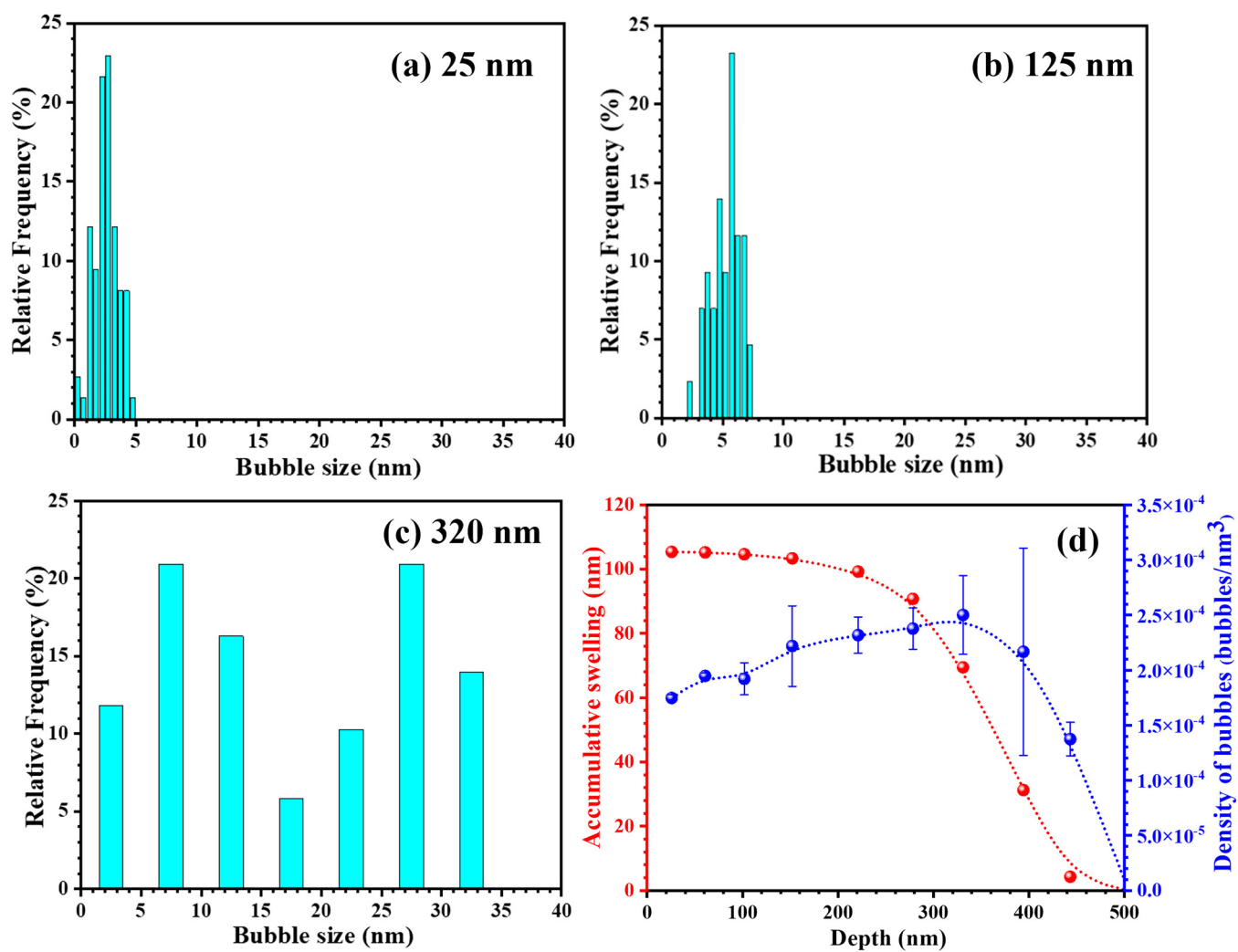


FIG. 6. The cross-sectional micrographs and corresponding SAED patterns of Si (001) implanted with  $1.0 \times 10^{18}$  ions/cm<sup>2</sup>: (a) low magnification TEM image of the implanted area; (b) the enlarged image of position (b) marked in image (a); and (c)–(e) the SAED patterns at different positions.

concentration. SAED patterns also illustrate the depth position at which a transition from crystalline to amorphous in Si (100) is occurred, as shown in Figs. 6(c)–6(e). Comparing fluences, implantation with a fluence of  $1.0 \times 10^{17}$  ions/cm<sup>2</sup> produces partial amorphization, while an implantation fluence of  $1.0 \times 10^{18}$  ions/cm<sup>2</sup> exhibits total amorphization. In addition, the thickness of the amorphous layer increases with implantation fluences, as shown in Figs. 5 and 6.

Figure 7 exhibits the experimental results of the bubble diameter distribution, bubble density, and cumulative swelling height as a function of implantation depth for the fluence of  $1.0 \times 10^{18}$  ions/cm<sup>2</sup>. The bubble formation extends to the implanted surface from one side and to the maximum implantation depth approaching uniform and small, while becoming non-uniform and larger at the

implantation depth from 201.0 to 382.0 nm. According to Figs. 7(a)–7(c), the smallest average bubble diameter is  $2.3 \pm 0.6$  nm approaching the surface, and the largest bubble diameter reaches up to  $17.2 \pm 9.89$  nm at the depth of 320.0 nm. The average values reported here are based on 20 TEM images. Furthermore, the bubble density profile follows a similar trend to the average diameter of bubble distribution. In addition, the void swelling in Si follows nearly a Gaussian distribution with a maximum volumetric swelling around 0.022 at the depth of 320 nm. The method employed to calculate the volumetric swelling of Si is adopted from Ref. 42. Leclerc *et al.* investigated the swelling behavior of SiC under helium implantation and proposed that amorphization and helium bubbles are the main reasons to cause the swelling.<sup>28</sup> Furthermore, Yang *et al.* proposed that the swelling height caused



24 August 2020; 06:54:15

**FIG. 7.** Bubble size distribution, bubble density, and cumulative swelling height resolved in depth for the fluence of  $1.0 \times 10^{18}$  ions/cm<sup>2</sup>. (a)–(c) bubble size distribution at different depths and (d) bubble density and cumulative swelling height.

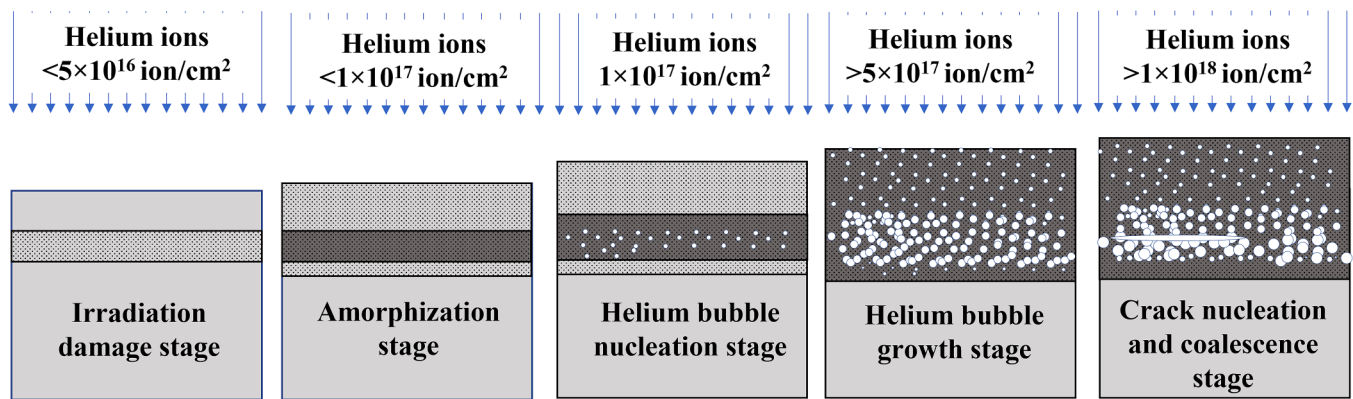


FIG. 8. Schematic cartoon of the structure and swelling evolution of helium implanted Si as a function of fluences.

by the helium bubbles can be calculated by using fractal volumetric swelling.<sup>43</sup> The cumulative swelling height of Si calculated from Yang's model as a function of implantation depth is also illustrated in Fig. 7. The calculated swelling height for samples implanted with the fluence of  $1.0 \times 10^{18}$  ions/cm<sup>2</sup> is about 105.4 nm based on Yang's model,<sup>43</sup> which is slightly higher than the height measured by AFM (97 nm), as shown in Fig. 2. The reason for the different swelling heights measured by TEM and AFM is attributed to the heterogeneous distribution of bubbles in Si along with the implantation depth, as shown in Fig. 7. It is noted that the size distribution of the bubbles is a bimodal distribution at the high fluence region, especially at the peak values of He concentration/dpa, as shown in Fig. 7(c). For simplicity, we utilize the average bubble

diameter to calculate the accumulative swelling in the current investigation, realizing that this might lead to a small overestimation of swelling height.

Based on the above results and statements, it can be found that in current experiments, the microstructure of Si under He implantation is determined by the fluences. Therefore, the damage process can be divided into different states based on the alternation of microstructure and fluences, including irradiation damage stage, amorphization stage, He bubble nucleation stage, He bubble growth stage, and stage of crack nucleation and coalescence. The structural changes, as well as swelling as a function of fluences, are schematically displayed in Fig. 8. In the irradiation damage state, in which the implantation fluence is less than  $5.0 \times 10^{16}$  ions/cm<sup>2</sup>, irradiation

24 August 2023 06:54:15

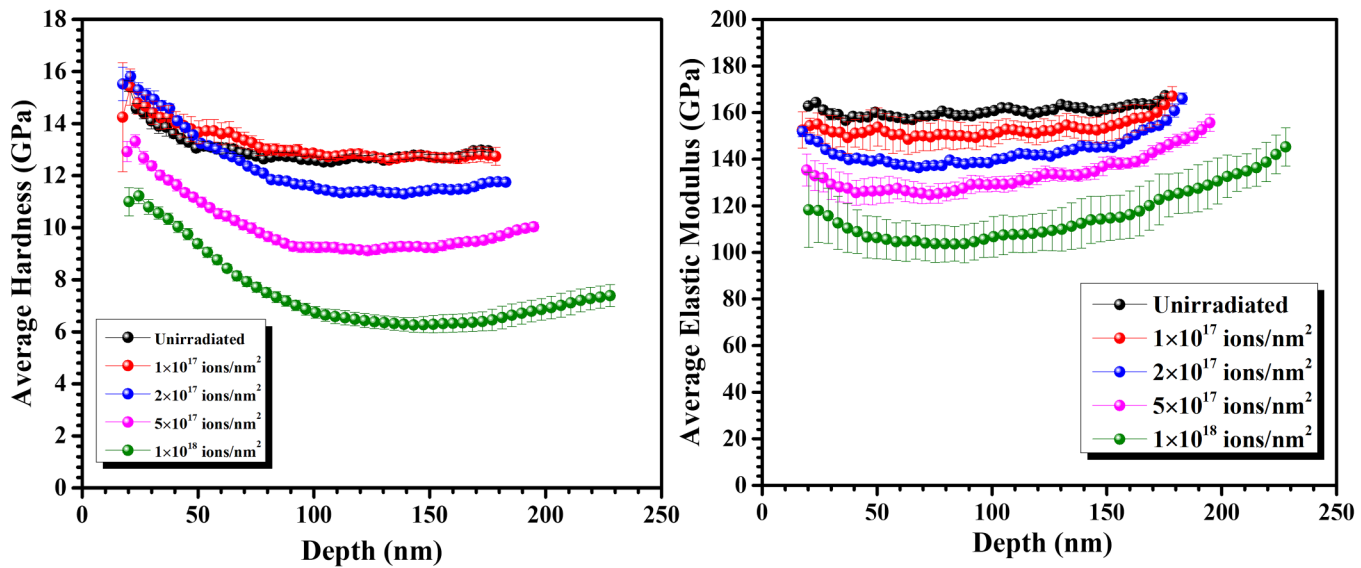


FIG. 9. Average hardness (left) and average reduced modulus (right) variation with depth for different implantation fluences.

induces the generation of defects, including interstitial clusters and vacancies, instead of the formation of bubbles and amorphization, as shown in Fig. 3. With the increase of fluences from  $5.0 \times 10^{16}$  to less than  $1.0 \times 10^{17}$  ions/cm<sup>2</sup>, the damage process gets into the amorphization stage, in which irradiation induced the formation of an amorphous layer in Si, as shown in Fig. 4. Because the binding energy between atoms is reduced by amorphization, the bubbles are easier to nucleate in the amorphous region. With the further rising of implantation fluences, more than  $7.5 \times 10^{17}$  ions/cm<sup>2</sup>, the entire implanted region gradually becomes amorphous. Meanwhile, the size of the bubble gradually increases with the increase of fluences. However, the heterogeneous distribution of bubbles in size and density along the implantation depth is formed because of the stopping of the helium ions at the end of the range, as shown in Fig. 5. The size of voids gradually increases with the further increase of fluences. The voids will merge together and then a crack will be formed when the fluence increases to more than  $1.0 \times 10^{18}$  ions/cm<sup>2</sup>.<sup>44</sup>

Average hardness and reduced modulus variation with depth of samples with and without implantation are illustrated in Fig. 9.

The results illustrate, as expected, that the average reduced modulus gradually decreases as the implantation fluence rises. Average reduced modulus for fluences of  $1.0 \times 10^{18}$ ,  $5.0 \times 10^{17}$ ,  $2.0 \times 10^{17}$ , and  $1.0 \times 10^{17}$  ions/cm<sup>2</sup> are about  $106.7 \pm 8.7$ ,  $129.4 \pm 3.1$ ,  $140.0 \pm 1.8$ , and  $150.5 \pm 5.1$  GPa reported at depth of around 100 nm, respectively, which are smaller than that of the unirradiated sample with  $160.9 \pm 1.2$  GPa. This result is widely consistent with results on self-ion implanted Si by Follstaedt *et al.*, who reported a reduced hardness and elastic modulus after implantation.<sup>45</sup> The Si is completely amorphous after 50 dpa of implantation and thus the elastic modulus is between 130 and 140 GPa depending on the substrate orientation. This result is slightly higher than our current samples implanted with  $5.0 \times 10^{17}$  ions/cm<sup>2</sup>, which the peak dose is around 50 dpa, because no bubbles are formed after self-ions implantation. In addition, the average reduced modulus gradually increases with the increase of penetration depth, which may be caused by the effect of the substrate beneath the implantation layer. It is generally accepted that the elastic modulus of materials will not change significantly with the alteration of the

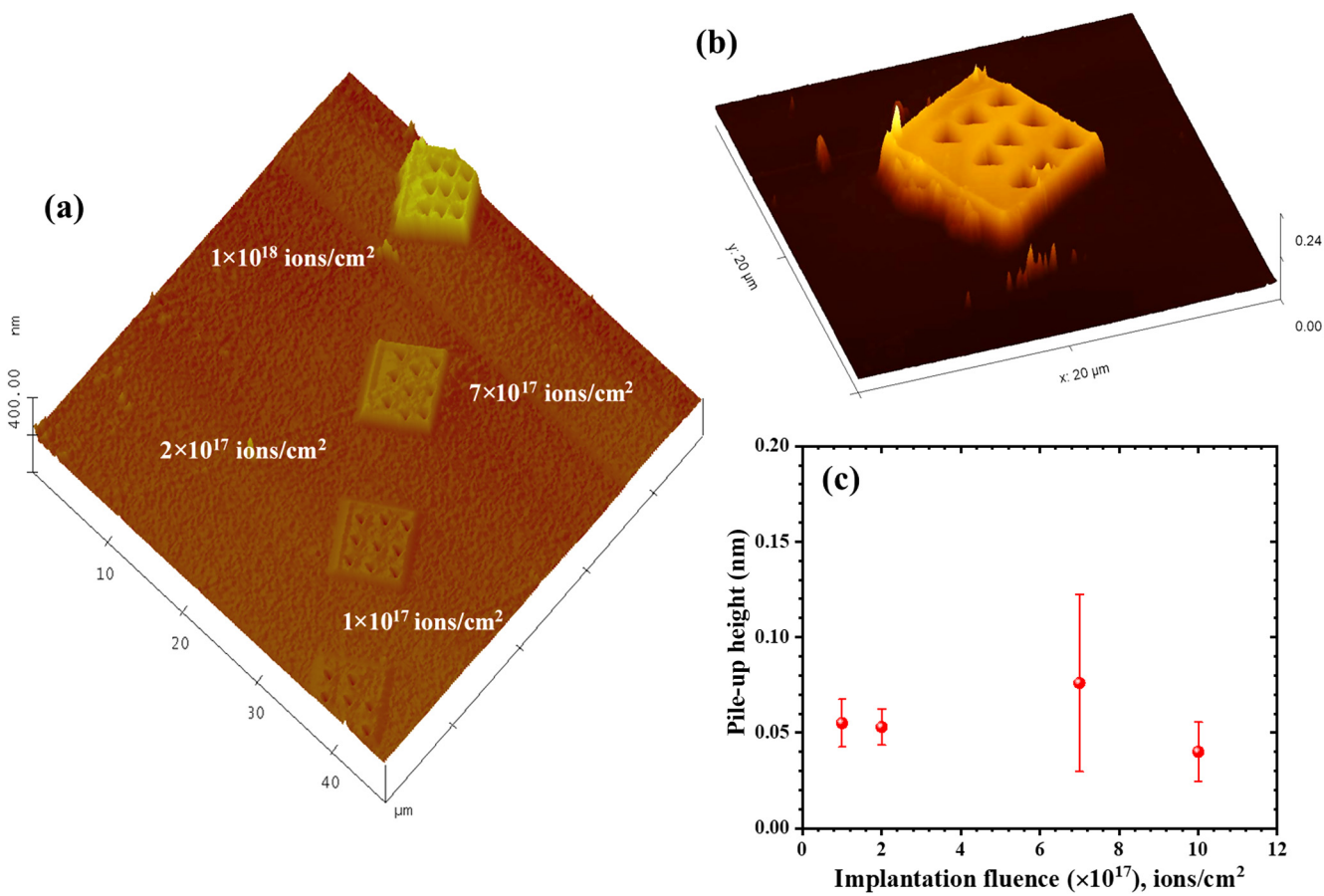


FIG. 10. The AFM surface topographic image of implanted areas and corresponding pileup height: (a) AFM image of irradiated area; (b) the enlarged AFM image of area implanted with  $1 \times 10^{18}$  ions/cm<sup>2</sup>; and (c) the relationship between pileup height and implantation fluence.

indentation depth as it is assumed to be a structure-insensitive property.<sup>46</sup> However, for implanted samples, the reduced modulus first declines with depth and then rises and approaches bulk values at deep penetration. The explanation for this phenomenon is the fact that both amorphization of the Si and the development of He bubbles reduce the overall elastic modulus.<sup>43</sup> In addition, other work assumed that the plastic deformation zone beneath the indentation can be approximated as a hemisphere with a radius of five to ten times the penetration depth.<sup>47,48</sup> Using this assumption in the current experiments, the plastic zone gradually expands into the unirradiated Si substrate with increasing of the penetration depth, resulting in a gradual increase of the elastic modulus back to the bulk property of 161 GPa at deep indentation depths.

With regard to the average hardness, however, it first increases before declining with increased implantation fluences at the depths below 75 nm. Average hardness for fluences of  $1.0 \times 10^{18}$ ,  $5.0 \times 10^{17}$ ,  $2.0 \times 10^{17}$ , and  $1.0 \times 10^{17}$  ions/cm<sup>2</sup> and unimplanted sample are  $9.4 \pm 0.2$ ,  $11.0 \pm 0.2$ ,  $13.3 \pm 0.1$ ,  $13.7 \pm 0.4$ , and  $13.1 \pm 0.2$  GPa, respectively. When penetration depth extends to more than 75 nm, there is no obvious difference between unimplanted and implanted samples with  $1.0 \times 10^{17}$  ions/cm<sup>2</sup> in terms of the average hardness measurement. However, the average hardness gradually declines with the further rising of implantation fluences due to the microstructure changes of Si. In addition, a decrease in hardness with increasing indent depth is observed. Such depth dependent hardness behavior is attributed to the indentation size effect (ISE) phenomena.<sup>49</sup> The AFM surface topographic image of implanted areas with different implantation fluences after nanoindentation testing is shown in Figs. 10(a) and 10(b). In addition, the relationship between pileup height and implantation fluence is also illustrated in Fig. 10(c). The results indicate that no significant change in a pileup or sink-in behavior as a function of fluence is observed. It is well known that the irradiation induced hardening behavior of materials is primarily attributed to the irradiation induced defects.<sup>50</sup> For Si implanted with a low fluence, for example,  $1.0 \times 10^{17}$  ions/cm<sup>2</sup>, the diameter of bubbles is small, and the implantation layer is not completely transformed from a crystalline to an amorphous state. Therefore, irradiation induced hardening behavior mainly can be associated with the bubbles and defect clusters rather than irradiation induced amorphization. As the size of bubbles gradually increases with the rising of implantation fluence, the irradiation induced defects effect gradually diminishes because they get absorbed by the bubble boundaries.<sup>51</sup> But even the large He bubbles still contribute to the hardness increase of Si-based on the Orowan model.<sup>52</sup> However, when implantation fluence increases to  $2.0 \times 10^{17}$  ions/cm<sup>2</sup>, as shown in Fig. 9, the hardness reduced significantly. A similar behavior was reported by Xu *et al.*, who investigated the hardening behavior of 6H-SiC under Ne<sup>8+</sup> ion irradiation, and they attributed this phenomenon to the dose threshold of lattice amorphization in SiC irradiated at RT.<sup>53</sup> With further increase of implantation fluence, a softening behavior in hardness is observed because an amorphized layer is formed and the size of bubbles approaches a critical value.<sup>53,54</sup>

#### IV. CONCLUSIONS

In the present work, the relationship between the swelling behavior, microstructure, and micromechanical properties of

Si (100) under 25 keV He implantation with different fluences at RT was investigated. The conclusions are as follows:

- (1) The swelling height gradually increases with the rising of implantation fluence, and their relationship follows a linear law. No blistering is observed even as implanted fluence is extended to  $1.0 \times 10^{18}$  ions/cm<sup>2</sup>.
- (2) Interstitial clusters rather than He bubbles are visible in bright-field TEM images of Si implanted with fluences of  $5.0 \times 10^{16}$  ions/cm<sup>2</sup>. A mixed layer consisting of amorphous and matrix with small size bubbles is observed at a fluence of  $1.0 \times 10^{17}$  ions/cm<sup>2</sup>. As the fluence reaches  $1 \times 10^{18}$  ions/cm<sup>2</sup>, a completely amorphous layer with a larger number of bubbles is observed. The density and average diameter of bubbles close to the implanted surface and to the maximum implantation depth is uniform and small, while bubbles are non-uniform and large in the middle of the implantation layer. The swelling and property change due to helium implantation is a mixture between amorphization, helium bubble formation, and vacancy concentration.
- (3) The average reduced modulus gradually declines with implantation fluence due to the reduction of the density of the implantation layer, while the average hardness goes through a maximum.

#### ACKNOWLEDGMENTS

This publication was made possible in part by NSF/DMRMRRI1338139. The research was performed using funding received from the National Science Foundation's Division of Materials Research, USA under Award No. 1807822. The samples were FIB-milled and He-implanted at the Biomolecular Nanotechnology Center/QB3 at UC Berkeley. The TEM was performed at the Molecular Foundry, which is supported by the Office of Science, Office of Basic Energy Sciences, of the U.S. Department of Energy under Contract No. DE-AC02-05CH11231.

#### AUTHOR DECLARATIONS

##### Conflict of Interest

The authors have no conflicts to disclose.

##### Ethics Approval

Ethics approval is not required.

##### Author Contributions

**Xi Huang:** Data curation (lead); Formal analysis (lead); Investigation (lead); Project administration (equal); Writing – original draft (lead). **Yujun Xie:** Data curation (equal); Formal analysis (equal); Investigation (equal); Methodology (equal); Resources (equal); Software (equal); Validation (equal); Visualization (equal); Writing – review and editing (equal). **Mehdi Balooch:** Conceptualization (equal); Data curation (equal); Investigation (equal); Methodology (equal); Resources (equal); Supervision (equal); Validation (equal); Visualization (equal); Writing and review and editing (equal). **Sean Lubner:** Formal analysis (equal);

Resources (equal); Writing – review and editing (equal). **Peter Hosemann:** Conceptualization (equal); Data curation (equal); Formal analysis (equal); Funding acquisition (equal); Investigation (equal); Methodology (equal); Project administration (equal); Resources (equal); Software (equal); Supervision (equal); Validation (equal); Visualization (equal); Writing – review and editing (equal).

## DATA AVAILABILITY

The data that support the findings of this study are available within the article and from the corresponding authors upon reasonable request.

## REFERENCES

- <sup>1</sup>G. S. Was, Z. Jiao, E. Getto, K. Sun, A. M. Monterrosa, S. A. Maloy, O. Anderoglu, B. H. Sencer, and M. Hackett, *Scr. Mater.* **88**, 33 (2014).
- <sup>2</sup>B. Heidrich, S. M. Pimblott, G. S. Was, and S. Zinkle, *Nucl. Instrum. Methods Phys. Res. B* **441**, 41 (2019).
- <sup>3</sup>J. S. Williams, *Mater. Sci. Eng. A* **253**, 8 (1998).
- <sup>4</sup>S. J. Pearton, *Mater. Sci. Rep.* **4**, 313 (1990).
- <sup>5</sup>M. Maldovan, *Nat. Mater.* **14**, 667 (2015).
- <sup>6</sup>J. Maire, R. Anufriev, R. Yanagisawa, A. Ramiere, S. Volz, and M. Nomura, *Sci. Adv.* **3**, e1700027 (2017).
- <sup>7</sup>M. Nomura, J. Shiomi, T. Shiga, and R. Anufriev, *Jpn. J. Appl. Phys.* **57**, 080101 (2018).
- <sup>8</sup>W. Wesch, *Nucl. Instrum. Methods Phys. Res. B* **68**, 342 (1992).
- <sup>9</sup>W. Wesch, E. Wendler, and C. S. Schnohr, *Nucl. Instrum. Methods Phys. Res. B* **277**, 58 (2012).
- <sup>10</sup>C. C. Griffioen, J. H. Evans, P. C. De Jong, and A. Van Veen, *Nucl. Instrum. Methods Phys. Res. B* **27**, 417 (1987).
- <sup>11</sup>B. S. Li, Y. Y. Du, Z. G. Wang, T. L. Shen, Y. F. Li, C. F. Yao, J. R. Sun, M. H. Cui, K. F. Wei, H. P. Zhang, Y. B. Shen, Y. B. Zhu, and L. L. Pang, *Nucl. Instrum. Methods Phys. Res. B* **337**, 21–26 (2014).
- <sup>12</sup>P. F. P. Fichtner, J. R. Kaschny, R. A. Yankov, A. Mücklich, U. Kreißig, and W. Skorupa, *Appl. Phys. Lett.* **70**, 732 (1997).
- <sup>13</sup>E. Oliviero, M. F. Beaufort, and J. F. Barbot, *J. Appl. Phys.* **90**, 1718 (2001).
- <sup>14</sup>D. L. da Silva, P. F. P. Fichtner, M. Behar, A. Peeva, R. Koegler, and W. Skorupa, *Nucl. Instrum. Methods Phys. Res. B* **190**, 756 (2002).
- <sup>15</sup>W. T. Han, H. P. Liu, and B. S. Li, *Appl. Surf. Sci.* **455**, 433 (2018).
- <sup>16</sup>J. H. Evans, *Nucl. Instrum. Methods Phys. Res. B* **196**, 125 (2002).
- <sup>17</sup>X. Cheng, Z. Feng, C. Li, C. Dong, and X. Li, *Electrochim. Acta* **56**, 5860 (2011).
- <sup>18</sup>M. Ikeyama, K. Saitoh, S. Nakao, H. Niwa, S. Tanemura, Y. Miyagawa, and S. Miyagawa, in *1998 International Conference on Ion Implantation Technology Proceedings (Cat. No.98EX144)* (IEEE, 1999), pp. 736–739.
- <sup>19</sup>P. K. Giri, V. Raineri, G. Franzo, and E. Rimini, *Phys. Rev. B* **65**, 012110 (2001).
- <sup>20</sup>S. Momota, J. Zhang, T. Toyonaga, H. Terauchi, K. Maeda, J. Taniguchi, T. Hirao, M. Furuta, and T. Kawaharamura, *J. Nanosci. Nanotechnol.* **12**, 552 (2012).
- <sup>21</sup>J. Zhang, S. Momota, T. Toyonaga, H. Terauchi, F. Imanishi, and J. Taniguchi, *Nucl. Instrum. Methods Phys. Res. B* **282**, 17 (2012).
- <sup>22</sup>T. Wirtz, P. Philipp, J.-N. Audinot, D. Dowsett, and S. Eswara, *Nanotechnology* **26**, 434001 (2015).
- <sup>23</sup>S. Agarwal, Y. Lin, C. Li, R. E. Stoller, and S. J. Zinkle, *Nucl. Instrum. Methods Phys. Res. B* **503**, 11 (2021).
- <sup>24</sup>J. Chang, J. Y. Cho, C. S. Gil, and W.-J. Lee, *Nucl. Eng. Technol.* **46**, 475 (2014).
- <sup>25</sup>P. Reinke, G. Francz, P. Oelhafen, and J. Ullmann, *Phys. Rev. B* **54**, 7067 (1996).
- <sup>26</sup>J. D. Arregui-Mena, T. Koyanagi, E. Cakmak, C. M. Petrie, W.-J. Kim, D. Kim, C. P. Deck, C. Sauder, J. Braun, and Y. Katoh, *Compos. B Eng.* **238**, 109896 (2022).
- <sup>27</sup>K. M. Tynyshbayeva, K. K. Kadyrzhanov, A. L. Kozlovskiy, Y. I. Kuldeyev, V. Uglov, and M. V. Zdorovets, *Crystals* **12**, 239 (2022).
- <sup>28</sup>S. Leclerc, A. Declémé, M. F. Beaufort, C. Tromas, and J. F. Barbot, *J. Appl. Phys.* **98**, 113506 (2005).
- <sup>29</sup>S. Eichler, J. Gebauer, F. Börner, A. Polity, R. Krause-Rehberg, E. Wendler, B. Weber, W. Wesch, and H. Börner, *Phys. Rev. B* **56**, 1393 (1997).
- <sup>30</sup>R. Nipoti, G. Lulli, S. Milita, M. Servidori, C. Cellini, and A. Carnera, *Nucl. Instrum. Methods Phys. Res. B* **112**, 148 (1996).
- <sup>31</sup>K. J. Abrams, J. A. Hinks, C. J. Pawley, G. Greaves, J. A. van den Berg, D. Eyidi, M. B. Ward, and S. E. Donnelly, *J. Appl. Phys.* **111**, 083527 (2012).
- <sup>32</sup>J. S. Custer, M. O. Thompson, D. C. Jacobson, J. M. Poate, S. Roorda, W. C. Sinke, and F. Spaepen, *Appl. Phys. Lett.* **64**, 437 (1994).
- <sup>33</sup>F. I. Allen, P. Hosemann, and M. Balooch, *Scr. Mater.* **178**, 256 (2020).
- <sup>34</sup>V. Raineri, S. Coffa, E. Szilágyi, J. Gyulai, and E. Rimini, *Phys. Rev. B* **61**, 937 (2000).
- <sup>35</sup>R. Siegele, G. C. Weatherly, H. K. Haugen, D. J. Lockwood, and L. M. Howe, *Appl. Phys. Lett.* **66**, 1319 (1995).
- <sup>36</sup>V. F. Reutov and A. S. Sokhatskii, *Tech. Phys. Lett.* **28**, 615 (2002).
- <sup>37</sup>M. L. David, M. F. Beaufort, and J. F. Barbot, *Nucl. Instrum. Methods Phys. Res. B* **226**, 531 (2004).
- <sup>38</sup>K. E. Haynes, “Defect evolution during elevated-temperature helium ion implantation into silicon,” Ph.D. thesis (University of Florida, 2019).
- <sup>39</sup>F. F. Morehead and B. L. Crowder, *Radiat. Eff.* **6**, 27 (1970).
- <sup>40</sup>V. Heera, F. Prokert, N. Schell, H. Seifarth, W. Fukarek, M. Voelskow, and W. Skorupa, *Appl. Phys. Lett.* **70**, 3531 (1997).
- <sup>41</sup>O. W. Holland, J. D. Budai, and C. W. White, *Appl. Phys. Lett.* **57**, 243 (1990).
- <sup>42</sup>M. Terasawa, M. Shimada, and S. Nakahigashi, *J. Nucl. Sci. Technol.* **19**, 646 (1982).
- <sup>43</sup>Y. Yang, D. Frazer, M. Balooch, and P. Hosemann, *J. Nucl. Mater.* **512**, 137 (2018).
- <sup>44</sup>X. Duo, W. Liu, S. Xing, M. Zhang, X. Fu, C. Lin, P. Hu, S. X. Wang, and L. M. Wang, *J. Phys. D: Appl. Phys.* **34**, 5 (2001).
- <sup>45</sup>D. M. Follstaedt, J. A. Knapp, and S. M. Myers, *J. Mater. Res.* **19**, 338 (2004).
- <sup>46</sup>P. Haußild, *J. Nucl. Mater.* **551**, 152987 (2021).
- <sup>47</sup>M. Mata, O. Casals, and J. Alcalá, *Int. J. Solids Struct.* **43**, 5994 (2006).
- <sup>48</sup>A. Katreer, A. Prasitthipayong, D. Krumwiede, D. M. Collins, P. Hosemann, and S. G. Roberts, *J. Nucl. Mater.* **498**, 274 (2018).
- <sup>49</sup>R. Kasada, Y. Takayama, K. Yabuuchi, and A. Kimura, *Fusion Eng. Des.* **86**, 2658 (2011).
- <sup>50</sup>R. Schaeublin, D. Gelles, and M. Victoria, *J. Nucl. Mater.* **307–311**, 197 (2002).
- <sup>51</sup>O. El-Atwani, J. E. Nathaniel, A. C. Leff, B. R. Muntfering, J. K. Baldwin, K. Hattar, and M. L. Taheri, *J. Nucl. Mater.* **484**, 236 (2017).
- <sup>52</sup>J. Gan and G. S. Was, *J. Nucl. Mater.* **297**, 161 (2001).
- <sup>53</sup>C. L. Xu, C. H. Zhang, J. J. Li, L. Q. Zhang, Y. T. Yang, Y. Song, X. J. Jia, J. Y. Li, and K. Q. Chen, *Nucl. Instrum. Methods Phys. Res. B* **286**, 129–133 (2012).
- <sup>54</sup>J. Li, H. Huang, G. Lei, Q. Huang, R. Liu, D. Li, and L. Yan, *J. Nucl. Mater.* **454**, 173 (2014).